View metadata, citation and similar papers at core.ac.uk

brought to you by CORE

provided by Explore Bristol Research

Oikonomidis, F., Shterenlikht, A., & Truman, C. E. (2013). Prediction of crack propagation and arrest in X100 natural gas transmission pipelines with the strain rate dependent damage model (SRDD). Part 1: A novel specimen for the measurement of high strain rate fracture properties and validation of the SRDD model parameters. International Journal of Pressure Vessels and Piping, 105, 60-68. DOI: 10.1016/j.ijpvp.2013.03.003

Peer reviewed version

License (if available):
Unspecified

Link to published version (if available):
10.1016/j.ijpvp.2013.03.003

Link to publication record in Explore Bristol Research
PDF-document

This is the author accepted manuscript (AAM). The final published version (version of record) is available online via Elsevier at doi:10.1016/j.ijpvp.2013.03.003. Please refer to any applicable terms of use of the publisher.

University of Bristol - Explore Bristol Research

General rights

This document is made available in accordance with publisher policies. Please cite only the published version using the reference above. Full terms of use are available:
http://www.bristol.ac.uk/pure/about/ebr-terms.html

Prediction of crack propagation and arrest in X100 natural gas transmission pipelines with the strain rate dependent damage model (SRDD). Part 1: a novel specimen for the measurement of high strain rate fracture properties and validation of the SRDD model parameters.

F Oikonomidis, A Shterenlikht, CE Truman

July 1, 2014

Abstract

A novel specimen for the measurement of strain rate and triaxiality dependent fracture properties of metals is described. The specimen is used in a conventional tensile split Hopkinson pressure bar test. The specimen is a flat 10mm wide and 1mm thick notched bar. Notch lengths between 2mm and 8mm were used. Several tests were performed on specimens cut from an X100 pipe at room temperature and strain rates up to $2000s^{-1}$. Finite element modelling of the stress-strain fields in the specimen immediately prior to crack propagation across the ligament was used to extract the flow properties, the damage initiation strain and the crack propagation energy as functions of stress triaxiality and strain rate. This data is used for tuning the strain rate dependent damage model (SRDD). The SRDD model was validated against the experiments and a good agreement was observed. In Part 2 of this paper the tuned SRDD model is used for the simulation of an axial crack propagation and arrest in pressurised natural gas pipelines. Very good agreement with the burst tests is observed, thus validating the utility of the proposed specimen design and of the SRDD model.

Keywords: dynamic fracture, Hopkinson bar, high strain rate, triaxility.

1 Introduction

Defects occurring in gas pipelines, either due to poor manufacture or harsh in service conditions, can lead to cracks. Cracks in such pipelines may lead to truly catastrophic fractures. A combination of high internal gas pressure and inertia of the opening crack flanks can result in cracks propagating for 20m and longer (see Fig. 1) at speeds of 200-300 m/s [1, 2].

Figure 1: An X100 pipe burst test result, from [3]. A fully ductile axial crack propagated for over 20m in this case.

Full scale burst test is the best way of assessing the crack propagation resistance of a natural gas pipeline. However, burst tests are very expensive and time consuming [3, 1, 4, 2], and cannot therefore be used routinely. To complement detailed but infrequent burst test assessment, the industry now routinely uses FEA structural integrity assessment.

Continuous ductile damage local approach models are successfully used in structural integrity assessment where the main risk is ductile crack propagation. Although traditionally applied to quasi-static analyses of bulk solids, there have been successful attempts in applying Gurson-Tvergaard-Needleman (GTN) model [5] to pipeline steels and/or geometries. [6] successfully analysed crack propagation in X60 and X65 pipeline steels on small specimens. [7] incorporated the Hill anisotropic yield criterion into the GTN plastic potential, and successfully predicted shear fracture propagating at 20-40 m/s on the round bars of X70 material. [8] used GTN model to pre-

dict burst pressure in X60 pipe, that agreed well with the experimentally measured value.

Despite considerable success in the application of GTN (and other) ductile damage models to structural integrity of pipelines, several problems remain. Transferability of tuned GTN parameters from notched to cracked geometries is still questionable. The requirement for very small finite element size in the process zone, comparable to a characteristic microstructural length scale, typically in the order of 50-200 μm, leads to extremely large number of elements in pipe models (unless the crack path is prescribed in advance). Finally there is an unresolved issue of the sensitivity of the GTN parameters to strain rate.

One alternative to continuous damage mechanics is the strain rate dependent damage (SRDD) model [9, 10, 11], which we examine in this work. This model was specifically formulated for thin structures. It is sensitive to strain rate and constraint. Finally, the model can be used with large shell finite elements. Shell elements in the order of 40mm were used successfully in [12], which, compared with 50-200μm element sizes required by continuum ductile damage models, leads to massive computational efficiency. All this potentially makes SRDD a preferred model for the simulation of axial ductile fracture propagation for long distances in large thin structures, such as pressure vessels and pipelines.

However, before the SRDD model can be used in a structural integrity assessment, it must be tuned for a range of strain rates and triaxiality levels for the target material. This is the focus of this paper.

The fact that stress triaxiality plays a prominent role in the onset of fracture has been known for a while. However, there is surprisingly little published work with experimental values of fracture strain as functions of triaxiality. By using a series of compressive, tensile and shear tests [13, 14] found that fracture strain in an aluminum alloy varies significantly with triaxiality. However, the authors had to use the average triaxiality value, because the level of triaxility changes during the test.

In part 1 of this paper we show that the parameters necessary to use the SRDD model can be measured on a small scale laboratory specimen, using high strain rate testing and a judicious application of finite element analysis. In part 2 of this paper we use the tuned SRDD model for a structural integrity assessment of pressurised natural gas pipelines. The SRDD model is applied to simulating axial crack propagation and arrest in X100 steel pipelines, and the results are compared against three burst test results published in open literature.

An X100 grade material is still relatively new in the UK and hence it was chosen for this study. It must be emphasised X100 API (American Petroleum Institute) grade line pipe steel is in fact a large class of steels, the only common feature of which is that the yield stress of the finished pipe must be above 100 kpsi (690 MPa). It is interesting to note that to achieve

this level of yield stress in the final product the plate or coil material prior to rolling into a tube and welding must have a substantially higher yield stress, sometimes as high as 130 kpsi (896 MPa).

The plan of part 1 of this paper is as follows. Section 2 gives the background of the SRDD model used in this work. Section 3 proposes a novel high strain rate specimen for the measurement of flow and the fracture characteristics of materials at high strain rates. In sections 4 and 5 we calculate the damage initiation strain and crack propagation energy. Finally sections 6 and 7 discuss the SRDD model validation and the advantages and the drawbacks of the proposed specimen and the high strain rate experiment. The paper is concluded in section 8 with useful recommendations for the future.

2 Strain rate dependent damage (SRDD) model

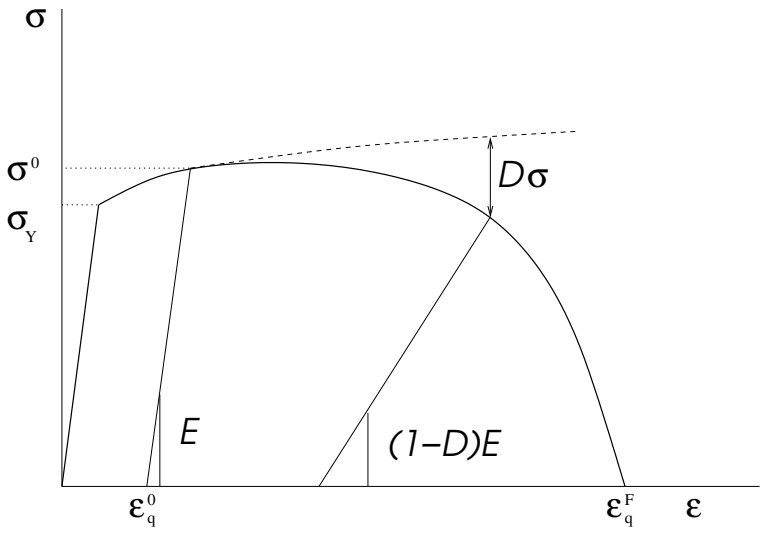

Figure 2: Schematic diagram of a damage model. σ_Y is the yield stress, σ_0 is the flow stress at which damage initiates, ε_q^0 is the equivalent plastic strain at which damage initiates, ε_q^F is the equivalent plastic strain at final fracture, D is the damage variable, $D = 0$ at damage initiation and $D = 1$ at final fracture. Up to damage initiation point the material stiffness is unchanged, E. As soon as damage initiates, the material stiffness is $(1 - D)E$, so that stiffness is zero at final fracture. The dashed line shows the flow curve in the absence of damage.

Fig. 2 illustrates a general idea behind a damage model. A complete damage model typically includes (1) elasto-plastic response of an undamaged material, (2) damage initiation criterion, and (3) damage evolution criterion.

All these can depend on strain rate, triaxiality, temperature, etc.

In this work we use a conventional damage initiation criterion [9, 10, 11]. Damage initiates when

$$\int \frac{\mathrm{d}\varepsilon_q}{\varepsilon_q^0(\eta, \dot{\varepsilon_q})} = 1 \tag{1}$$

where ε_q is equivalent plastic strain; ε_q^0 is the equivalent plastic strain at damage initiation; $\eta = -p/q$ is the triaxiality ratio, $p = -\sigma_{ii}$ is pressure, q is von Mises equivalent stress; and $\dot{\varepsilon_q}$ is the equivalent plastic strain rate.

Shear damage initiation was not used in this work, because measurement of shear stress ratio at high strain rates could not be achieved with our current experimental setup.

In this work we choose the onset of crack propagation in a notched specimen as the damage initiation point. The rationale for this choice is that crack tip necking will immediately preceed crack propagation.

Damage localisation is mesh dependent, i.e. the strain will localise in a single element, or in a single row of elements, so that with decreasing element size, the dissipated energy tends to zero. To avoid mesh dependence a characteristic length parameter, L, is introduced and stress-displacement relationship is used instead of the stress-strain relationship. Following [9] the crack propagation energy per unit surface area, G_F, is defined as:

$$G_F = \int_{\varepsilon_q^0}^{\varepsilon_q^F} L\sigma \mathrm{d}\varepsilon_q = \int_{u_q^0}^{u_q^F} \sigma \mathrm{d}u_q \tag{2}$$

where u_q is equivalent plastic displacement, u_q^0 is equivalent plastic displacement at damage initiation i.e. the appearance of necking, and u_q^F is equivalent plastic displacement at fracture. G_F is considered to be a material property.

In the experiments L was taken as the gauge length of the notched specimen, as will be explained in section 5. In finite element modelling, L was taken as the characteristic element size, or more precisely, as the distance between the relevant nodes in the element under analysis.

Various forms of the damage evolution law have been proposed in literature, e.g. linear and exponential. However, the key factor for this work is that all of them can be expressed in terms of G_F. In this work we used the exponential form of the softening law. The exponential form of the softening law is included in the Abaqus finite element code [11]. We have used the SRDD model in the Abaqus to predict the damage evolution in the high strain rate specimen and compare with the experimental measurements.

So, in order to use a damage model we need to experimentally measure $\sigma(\varepsilon_q, \dot{\varepsilon_q})$, $\varepsilon_q^0(\eta, \dot{\varepsilon_q})$ and G_F. The following sections will detail how these

properties were measured on X100 pipe material using a novel specimen design.

3 Specimen design for high strain rate testing

Split Hopkinson pressure bar (SHPB) is the most widely used test for the measurement of flow properties of materials at strain rates in the order of $10^3 s^{-1}$. The following section will briefly describe a tensile SHPB rig used for this work. For a more general introduction of the SHPB technique the reader is referred to [15, 16].

3.1 Details of the tensile SHPB rig at Bristol University

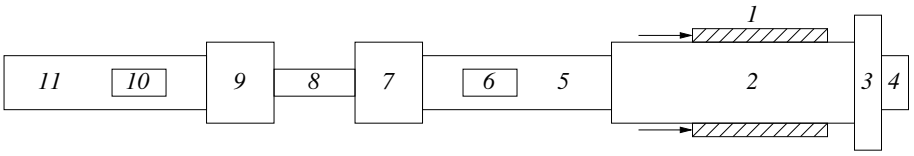

Figure 3: Schematic of tensile SHPB rig (not to scale), showing: (1) projectile, (2) loading bar, (3) transfer flange, (4) M20 bolt, (5) incident bar, (6) incident strain gauge, (7) and (9) two identical specimen holders, (8) specimen, (10) transmitted strain gauge, (11) transmitter bar.

Schematic of a tensile SHPB operation is shown in Fig. 3. A hollow projectile (1) is accelerated by pressurised nitrogen gas towards the transfer flange (3) upon the release of a solenoid valve. A transfer flange sits at the end of the loading bar (2), to which it is connected with M20 bolt (4) with a neck machined down to 15.8 mm in diameter. When the projectile comes into contact with the flange, tensile stress is suddenly transferred into the loading bar through the bolt thread. This starts a tensile pulse in the loading bar. At the same time under the action of this tensile stress the machined bolt will fracture. The point of bolt fracture determines the end of the tensile pulse. In this way a trapezoid-shaped tensile stress pulse is generated in the loading bar which travels along its length into the incident bar (5).

The tensile pulse is propagated through the specimen holder (7) into the specimen (8), and then through another specimen holder (9) and into the transmitter bar (11). The transmitted strain, ε_t, is registered by the transmitted strain gauge (10). Part of the tensile pulse is reflected at the specimen-holder interface (7-8) back into the incident bar as a compressive pulse, ε_r, and is registered by the incident strain gauge (6).

Using the one-dimensional wave propagation theory, the engineering strain and stress in the specimen can be calculated as [15, 16]:

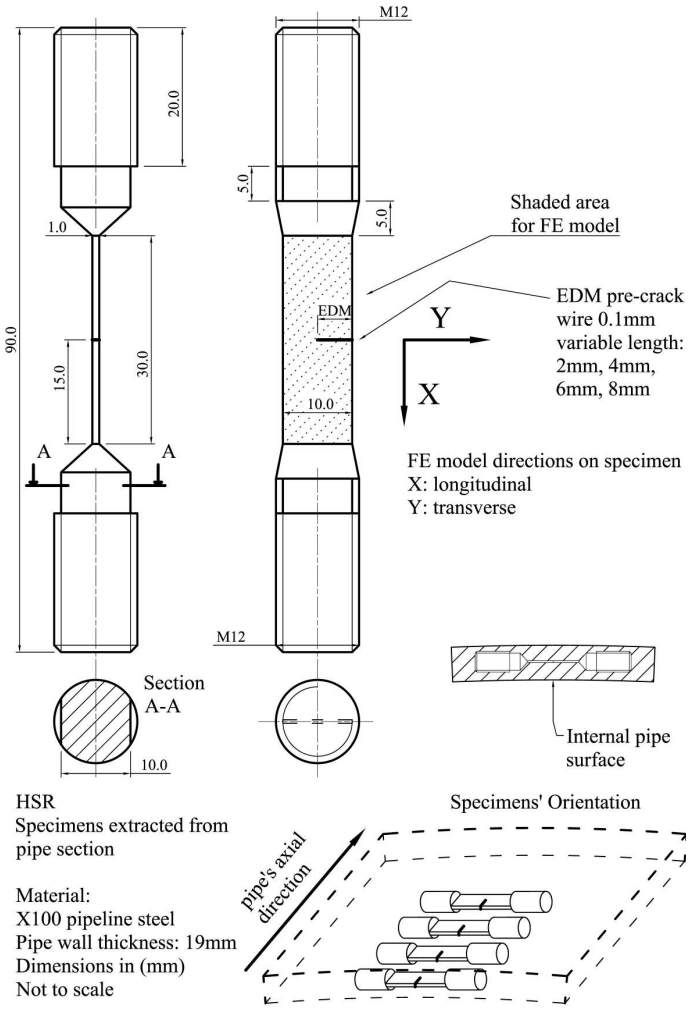

Figure 4: Notched SHPB specimen, showing the specimen dimensions and the orientation of the specimen wrt pipe geometry.

$$\varepsilon = -2\frac{C_B}{L^0}\int^t \varepsilon_r \mathrm{d}t \tag{3}$$

$$\sigma = \frac{A_B}{A_S^0} E_B \varepsilon_t \tag{4}$$

where C_B is the wave speed in the bar material, L^0 is the initial specimen gauge length, A_B is the cross section of the incident and the transmitter bars, A_S^0 is the initial cross section of the specimen, E_B is the Young's modulus of the bar material.

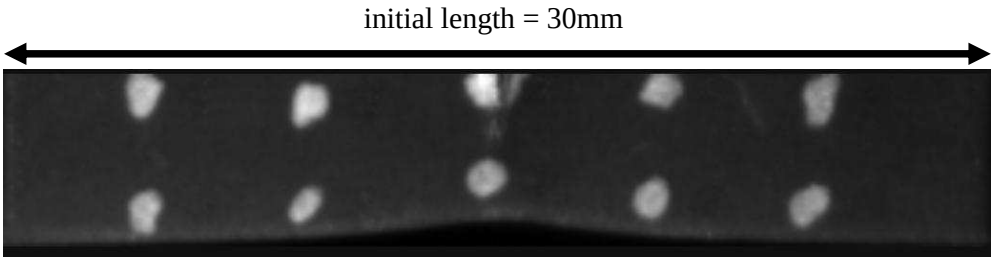

Figure 5: Markers drawn on the specimen surface for optical strain measurement, showing the moment immediately before the crack propagated fully through the specimen. Initial notch length was 2 mm. The notch tip is visible at the top of the image directly to the right of the middle marker.

3.2 Notched specimen design and measurement of flow properties

The specimen dimensions together with the cutting scheme are shown in Fig. 4. The specimens were machined directly from a 19 mm thick X100 pipe.

Typically round bars are used in SHPB experiments. In this work the gauge section was 10 mm wide and 1 mm thick with an EDM notch. This geometry was chosen because it achieves a range of stress triaxiality values ahead of the crack tip in a single specimen. Four specimens were tested with notch lengths of 2,4,6 and 8 mm, or equivalently with notch to width ratios of 0.2, 0.4, 0.6 and 0.8 respectively.

In addition, the flat faces of the gauge section were used for optical measurement of strain. To this end a pattern of markers was drawn on the specimen, see Fig. 5 Video recording was done at 400,000 frames per second. In each specimen the videos showed significant degree of plastic deformation (necking can be seen in Fig. 5) prior to fracture. However, the actual fracture propagation process was too quick to be captured in any detail even at this frame rate. We can conclude that the whole crack propagation process took less than 2.5 μs.

Engineering strain, ϵ_{eng}, was measured from the recorded images using Imetrum digital image correlation software [17]. Identical procedures were used for the testing and the analysis of all 4 specimens. Here we show the results for the 2mm notched specimen.

Figs. 6 and 7 show the stress-time and the strain-time signals respectively. The strain rate, found by a linear regression of the strain-time signal, is 1835 s^{-1} in this case. Fig. 8 shows the resulting engineering strain, ϵ_{eng}, vs engineering stress, σ_{eng}, curve. To find the true strain, ϵ, and the true stress, σ, a polynomial fit was used over the engineering stress-strain curve up to the maximum engineering stress, where it is assumed the necking

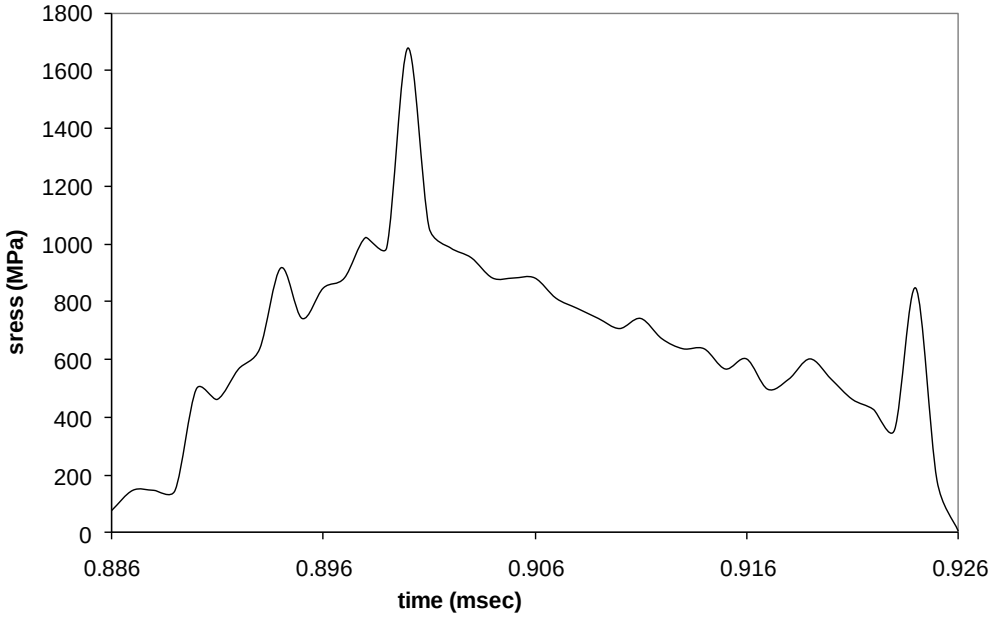

Figure 6: Stress-time plot for 2mm notched specimen. The final fracture strain was taken as the point where stress first hit zero.

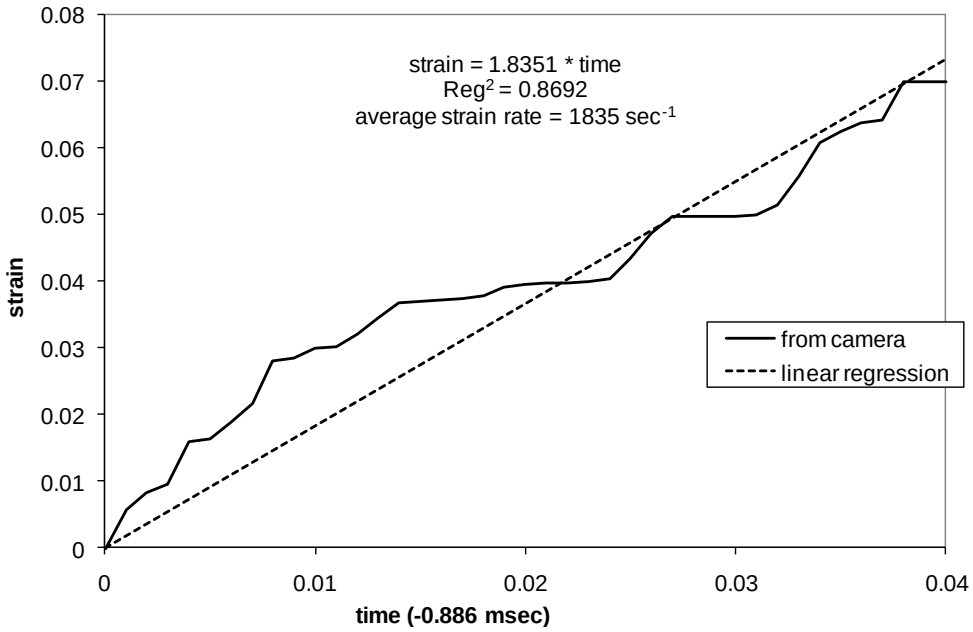

Figure 7: Strain-time plot for 2mm notched specimen.

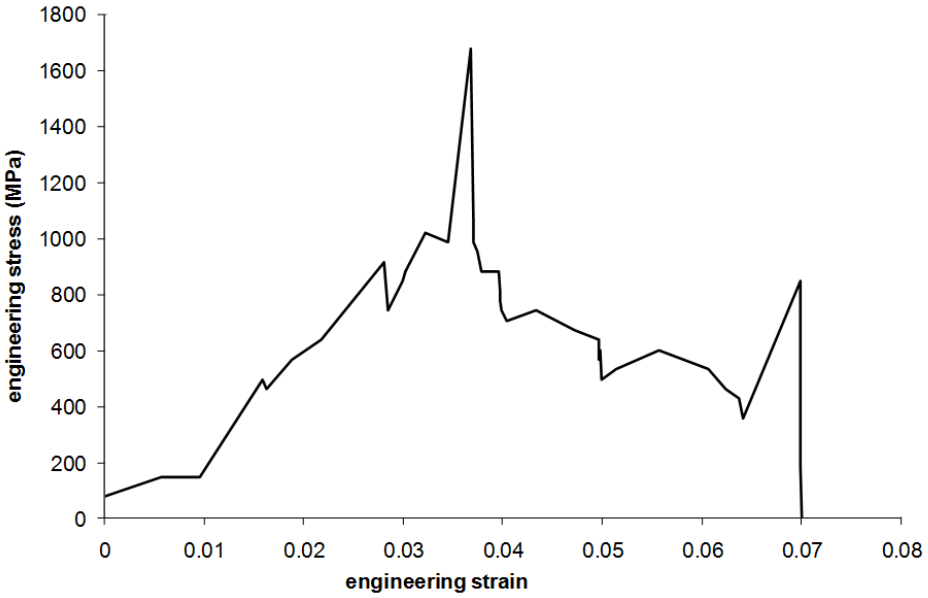

Figure 8: The measured stress-strain curve for 2mm notched specimen, strain rate of 1835 s^{-1}.

would occur. Then these expressions were used with the fitted engineering strain and stress: $\epsilon = \ln(1 + \epsilon_{\text{eng}})$, $\sigma = \sigma_{\text{eng}} \times (1 + \epsilon_{\text{eng}})$. **Note that these 1D expressions are only approximately valid for the notched geometry. However, because a more accurate conversion of engineering strain and stress into true quantities is significantly more complex, involving elasto-plasto-dynamic FE with yet unknown flow properties, it was decided to adopt an approximate but very cheap solution to keep the whole of the method practical.**

Beyond the point of the maximum engineering stress an incremental iterative fitting process was used. A trial true strain - true stress point was added to the flow curve and an FE simulation of the specimen was conducted with the aim of predicting the engineering stress and strain. The predicted engineering stress and strain were compared with the values from the polynomial fit, and the trial values for true stress and strain were adjusted. This process was continued until a good fit was achieved. Then the next true stress true strain trial point was chosen, and the iterative fitting process was repeated. The flow curves from all 4 specimens are given in Fig. 9. We note that the flow data for the strain rate of 1207s^{-1} is only slightly higher than the the quasi-static properties of this same X100 material reported in [18] as: yield stress of 750 MPa and UTS of 950 MPa.

Note that the strain rate cannot be prescribed directly in the split Hopkinson pressure bar experiment directly. Rather it is a results of the chosen firing gas pressure and the notch length. This data is shown in Table 1.

notch, mm	pressure, MPa	strain rate, s^{-1}
2	1.310	1835
4	1.310	2002
6	1.241	1700
8	1.186	1207

Table 1: The resulting strain rates as functions of the notch length and the gas firing pressure.

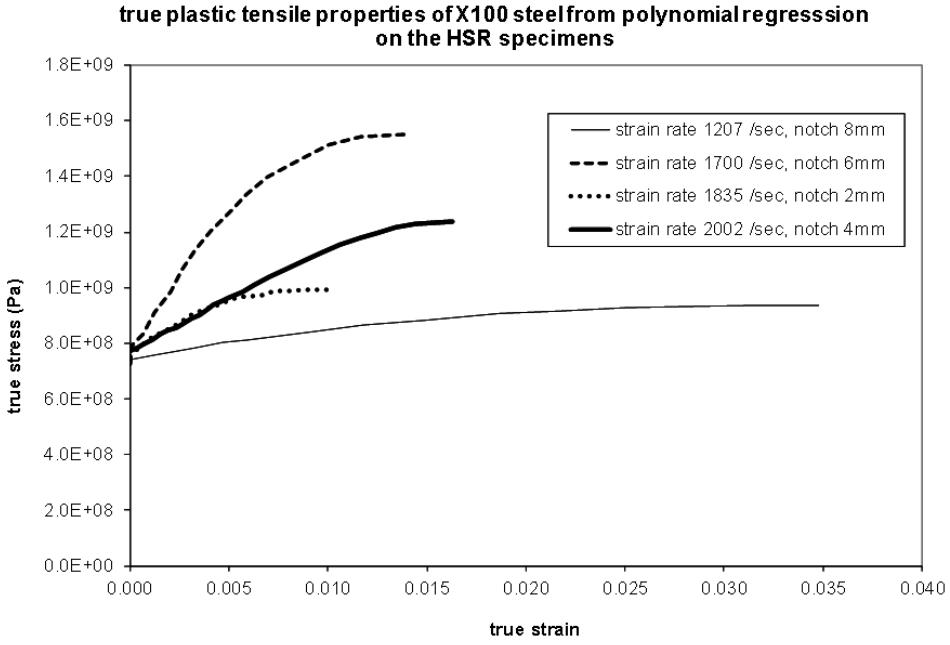

Figure 9: The measured stress-strain curve for all four notched specimens. Note that the curve for 1700 s^{-1} appears to be anomalous.

Finally Fig. 10 shows that even at the highest strain rate achieved in this work, $2002s^{-1}$, the fracture is fully ductile, and virtually the same as for the quasi-static fractures.

4 Calculation of damage initiation strain, as function of strain rate and triaxiality

2D plane stress finite element models of the specimen gauge section were created, see Fig. 11. The mesh size in the damage zone was 50μm. The models were loaded under displacement control. The maximum applied displacement at the boundary was such that the engineering strain over the whole length of the model was equal to the engineering fracture strain

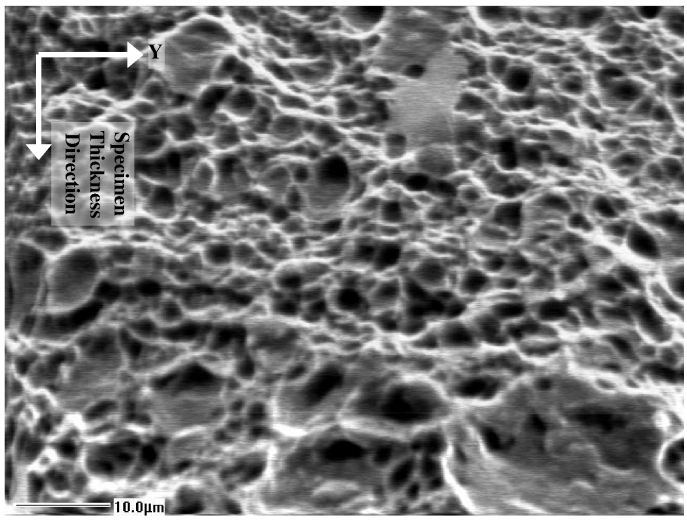

Figure 10: Scanning electron microscope image of the fracture surface of 4mm notch specimen, fractured at gauge strain rate of $2002s^{-1}$ at room temperature. Note the classical dimpled structure, indicative of a fully ductile fracture process, e.g. by void growth and coalescence.

measured in the experiment.

The dynamic flow properties, measured earlier, were used in the FE models. However, damage was not simulated. The aim of this FE modelling was to calculate stress triaxiality as a function of strain and strain rate. To this end the stress triaxiality and strain were calculated for each material point on a line normal to the notch, and located at half the remaining ligament width. The justification for this choice of stress triaxiality calculation is that the crack propagation process is so fast that from the onset of crack propagation, until the point at which the crack has run through the whole of the ligament and reached the other side, the global engineering strain, measured over the whole length of the specimen remained virtually unchanged. This means that when the models are under the maximum applied strain, the crack length could be anywhere between the initial value and the width of the specimen. Hence we take a mid point as an approximation of the crack tip position.

After [14] we have adopted the exponential form of the damage initiation strain, $\epsilon_0(\eta, \dot{\epsilon}_q)$, relationship:

$$\epsilon_0 = d_0 \exp(-3c\eta) + d_1 \exp(3c\eta) \tag{5}$$

where d_0, d_1 and c are three strain rate dependent material parameters fitted from experimental data. For each recorded value of strain rate these parameters were fitted using non-linear least squares minimisation from the calculated strain and triaxiality data. The best fitted parameters are shown

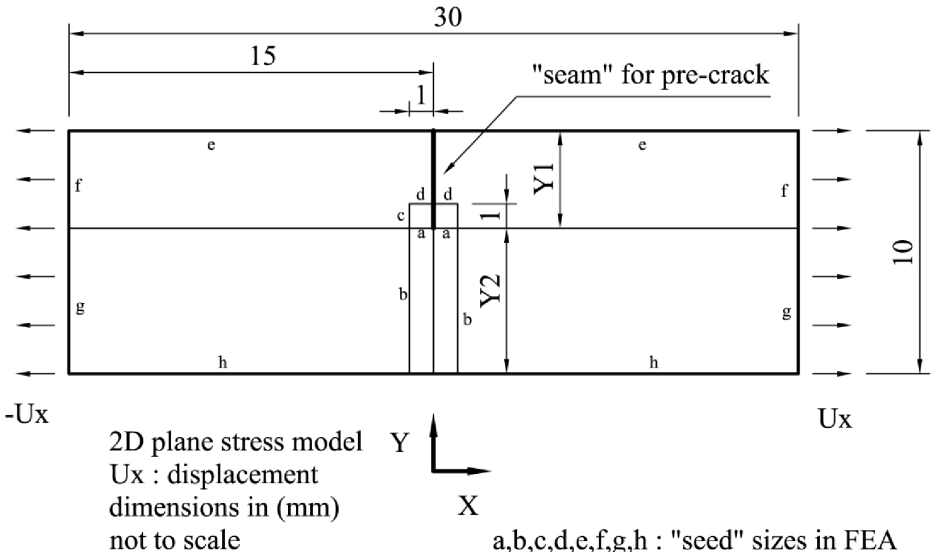

Figure 11: FE model of the SHPB specimen gauge section, showing the major dimensions and the boundary conditions.

in Table 2 and the resulting damage initiation curves are shown in Fig. 12.

All curves have a distinctive "U" shape. Generally, as would be expected, low triaxiality and low strain rate increase damage initiation strain. One interesting finding is that the minimum damage initiation strain of about 0.07 corresponds to a triaxiality ratio of 0.27-0.28, for all high strain rates under investigation. However, for lower and for higher triaxiality values, the damage initiation strain depends strongly on the strain rate. In addition, increase in damage initiation strain with high triaxiality levels, above 0.3, agrees well with results reported in [13] for an aluminium alloy. The significance of these curves is that the onset of softening can be modelled

strain rate, s^{-1}	d_0	d_1	c
0.0025	1.784×10^{-2}	3.098	-4.382
1207	0.3484	4.040×10^{-2}	2.883
1700	0.6154	1.584×10^{-2}	3.400
1835	0.7440	1.608×10^{-2}	3.521
2003	0.7892	1.210×10^{-2}	3.190

Table 2: Fitted material properties for the exponential damage initiation strain function, $\epsilon_0(\eta, \dot{\epsilon}_q)$.

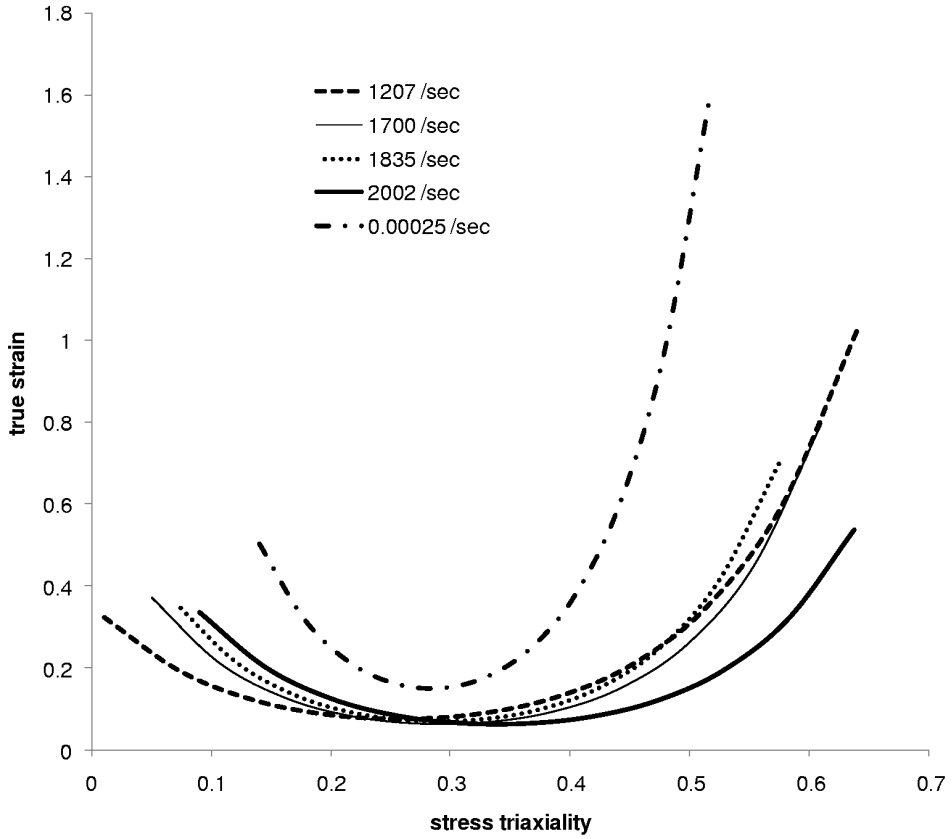

Figure 12: Damage initiation strain as a function of strain rate and stress triaxiality.

for a range of strain, strain rate and triaxiality values, irrespective of the finite element size. Thus the strain rate dependent damage model can be deployed with large element sizes, making analysis of large structures, for example pipes, more feasible.

It must be noted that the split Hopkinson bar theory is one-dimensional, whereas the stress and triaxiality distributions in our experiments are two-dimensional. Nevertheless, the current approach, with its inconsistencies, seems to be better than accepting a single average triaxiality value per specimen, as is the current practice suggested by [13].

5 Calculation of G_F

Triaxiality and strain rate dependence determine the onset of softening in the material. Once softening has started the material will absorb further energy, equivalent to G_F - the crack propagation energy per unit surface

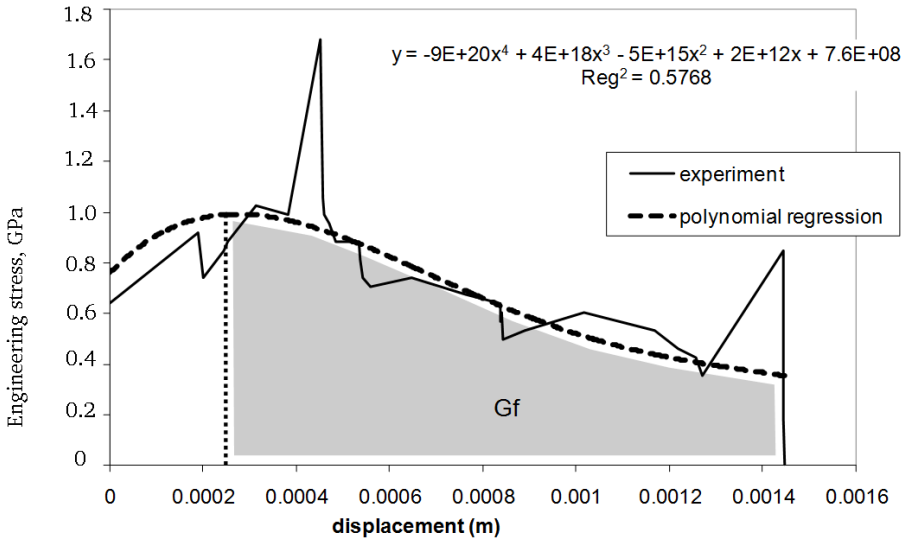

Figure 13: Polynomial fit over strain-displacement data for 2mm notched specimen, i.e. strain rate of 1835 s^{-1}. The area under the curve following the maximum stress is G_F=0.97 MJ/m^2.

area. Thus G_F determines the moment of final fracture of the material, after which it has no further load bearing capacity. In a finite element analysis the softening algorithm is applied to each element separately. Each element will absorb the amount of energy equal to G_F multiplied by its area. After that the finite element is removed from the mesh to avoid excessive mesh distortion.

G_F, was calculated as the area under the stress-displacement curve. First, a fourth order polynomial was fit over the experimental data. Then the area was calculated using the fitted curve, see Fig. 13.

The initial gauge length, 30mm (see Figs. 4 and 5) was used as the characteristic length, L, in eqn. (2). For the 2mm specimen, see Fig. 13, the limits of integration in eqn. (2) were $u_q^0 = 0$mm and $u_q^F = 1.45 - 0.25 = 1.2$mm. This displacement describes the plastic elongation of the gauge length beyond the necking point, which was obtained from the polynomial fit.

Significant strain rate dependence of G_F was observed, see Fig. 14, from 8.6 MJ/m^2 at 1207 s^{-1} down to 0.8 MJ/m^2 at 2002 s^{-1}. The average value is 3.5 MJ/m^2. We could not find any values for this or similar materials reported in open literature, hence we cannot report any comparisons.

Note that the theoretical formulation of G_F is one-dimensional, and therefore cannot take stress triaxiality into account. In the theoretical framework adopted here, the triaxiality affects only

damage initiation, and not damage evolution. However, because different notch lengths were used in these experiments, the separate effects of the strain rate and of different triaxiality on G_F cannot be separated. Therefore, we cannot claim conclusively that the variation in G_F shown in Fig. 14 is solely due to strain rate. More carefully controlled experiments are needed to fully separate the strain rate and the stress triaxiality effects.

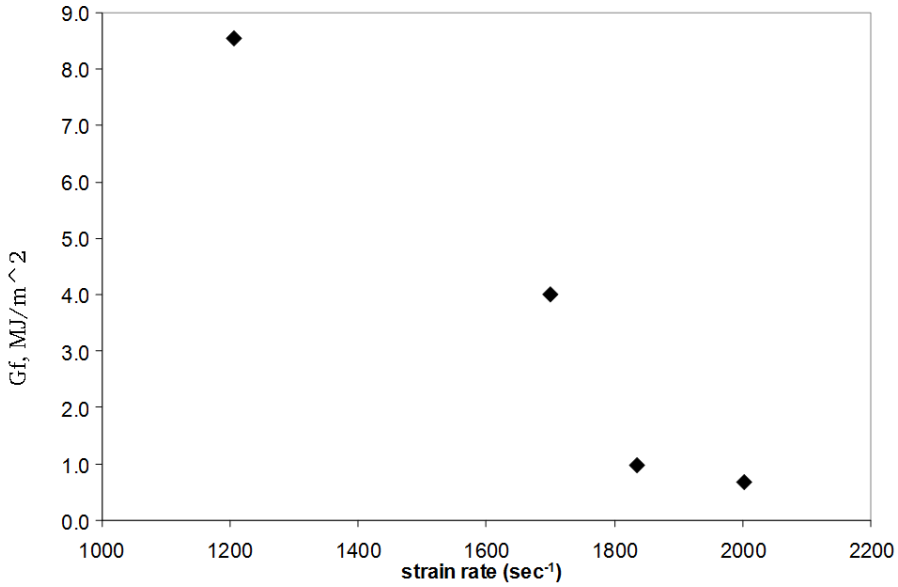

Figure 14: Fracture energy measured at 4 strain rates. Note significant strain rate dependence. **In accordance with the theoretical framework, see sec. 2, it is assumed that G_F is not affected by stress triaxility. However, see the text for more discussion on this point.**

Calculation of G_F is the final bit of data required for the use of the SRDD model.

6 Validation of SRDD model

Before applying the tuned SRDD model to the prediction of crack propagation in a natural gas pipeline (part 2 of this paper), the SRDD model was validated. The validation consisted of comparing the experimentally measured engineering failure strains in the high strain rate specimens with those predicted with SRDD model. Figs. 15 and 16 show the deformed mesh at final fracture and the experimental and modelling stress-strain curves for the 6mm notch specimen. The curves agree only partially. This is mainly due to the very noisy experimental stress signal, which is discussed in detail

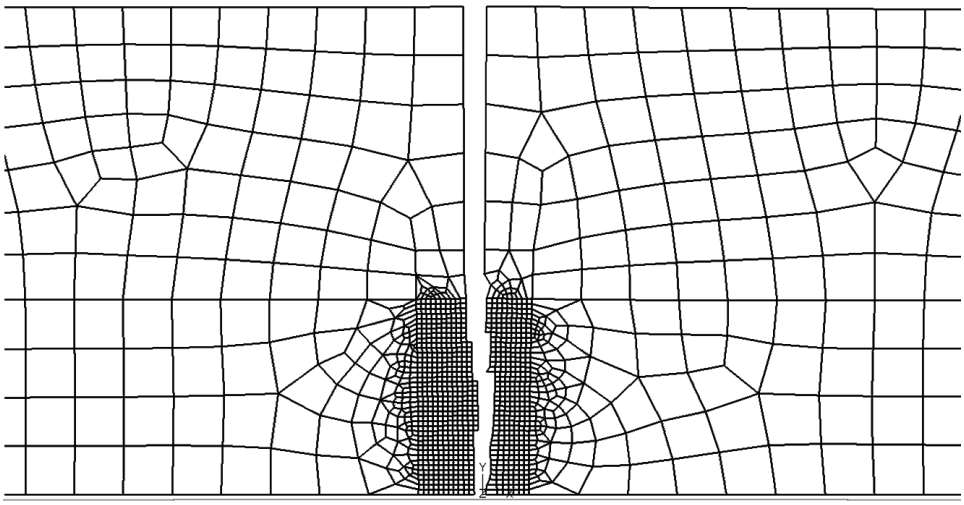

Figure 15: FE model of the high strain rate specimen with 6mm notch loaded at 1700 s^{-1} nominal strain rate, showing the deformed mesh at final fracture. Crack propagation was simulated with element deletion when the SRDD final fracture criterion was satisfied, i.e. when a FE element has absorbed energy equal to G_F times the element area. Note that the irregular crack path is that predicted by the model. The crack path is not pre-defined in advance.

in the next section. However, the maximum stress values do match. More importantly, the strain to failure was predicted correctly. The strain to failure determines element removal from the mesh, hence it is critical for the correct prediction of crack propagation in large structures.

7 Discussion

The approach to measuring fracture strain as a function of strain rate and triaxiality, adopted in this work, can be characterised as a hybrid experimental and modelling method. A flat notched specimen used in high strain rate experiments exhibits a range of stress triaxialities on a line normal to the crack plane, located mid ligament length. By accurately measuring the surface deformation of the specimen, the boundary conditions for the following finite element simulation of the stress distribution in the specimen are obtained. The outcome of the numerical modelling is a series of data points linking fracture strain with triaxiality for a particular value of strain rate. Hence, one of the major advantages of the proposed specimen and of the proposed method is that only a single specimen is required to measure fracture strain at a range of triaxiality values between 0 and 0.65. The easiest method for varying the applied strain rate is by changing the gas

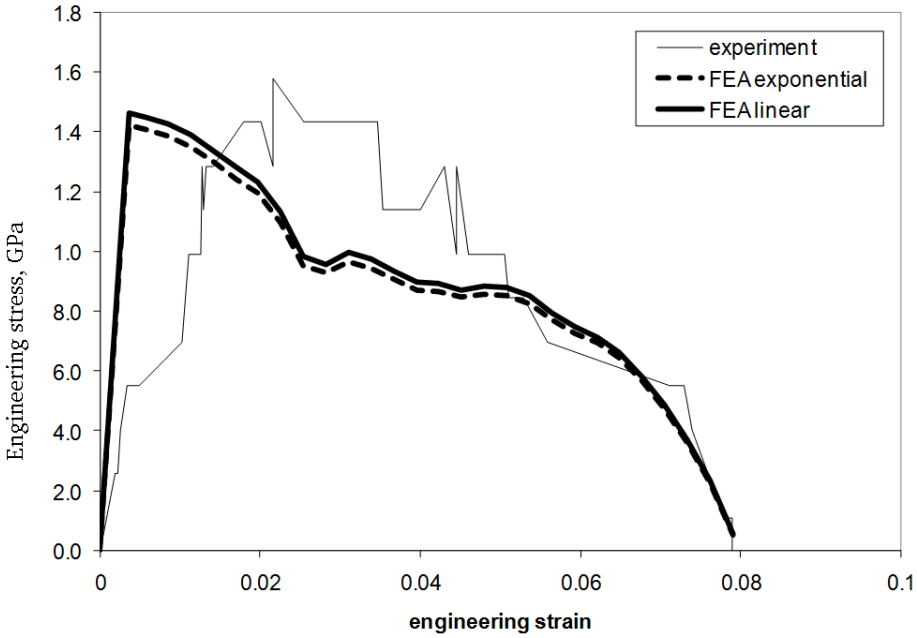

Figure 16: Experimental and modelling stress strain curves for 6mm notch specimen loaded at 1700 s^{-1} nominal strain rate. Note the excellent match of the failure strain.

firing pressure. In this case the notch length in the specimen can remain constant for all measurements. If, for some reason, gas firing pressure is hard to adjust, then different strain rates can be obtained by changing the notch length in the specimen or by changing the length of the input bar.

The effect of triaxility (and of the third stress invariant, in the form of the Lode angle parameter) on the ductile fracture strain has been studied extensively in [13, 14, 19, 20, 21], where the researchers took into account the evolution of these parameters during the whole of the deformation path leading to fracture. However, the approach taken in this work is different.

Because the fracture propagation in the proposed specimen is an extremely fast event, taking less than 2.5μs, it was not feasible to trace the evolution of stress triaxiality during crack propagation. Instead we we assumed that the onset of crack propagation is equivalent to final fracture, and hence used just the triaxility value corresponding to the moment at which crack was seen to move in the images recorded in the split Hopkinson bar experiments.

Also, because is proved impossible to measure local crack tip strain in experiments, with our current setup, we have used a global strain, measured over the gauge length of the specimen. Therefore we also used a global measure of triaxility, by calculating

its level on a line along the gauge length, i.e. normal to the crack propagation direction.

As in the previous published work [13, 14, 19, 20, 21], we have found a significant variation of fracture strain with triaxiality, however a direct comparison is not possible. This is partly due to the differences of approach, explained above, and partly due to the different focus of this and the prior research. We have concentrated on dynamic loading of X100 linepipe steel, whereas most of the published work was done in quasi-static experiments on various aluminium alloys and an austenitic steel.

The most important result from this work is shown in Fig. 12 - damage initiation strain as a function of stress triaxiality and strain rate. This data is somewhat contradictory. For stress triaxiality ratio of less than 0.28, damage initiation strain increases with strain rate. However, the trend is reversed when triaxiality is above 0.3. For all triaxiality values, the quasi-static damage initiation strain is significantly higher than any high strain rate value. Lack of a clear trend for all triaxiality values in Fig. 12 makes creation of a single $\varepsilon_q^0(\eta, \dot{\varepsilon_q})$ function for all η and $\dot{\varepsilon_q}$ hard. This will add complexity when using SRDD model for structural integrity calculations.

One specific distinguishing feature of the proposed specimen geometry is that it produces triaxiality of 0.64 immediately ahead of the crack tip. This value is very close to 0.6, which is the triaxiality calculated ahead of the propagating crack in a pressurised X100 steel pipeline, as shown in part 2 of this paper.

The signal/noise ratio for stress is poor, see Fig. 6. This is due to the impedance mismatch in the split Hopkinson bar experiment between the specimen and the incident and the transmitter bars. This effect is well known in wave propagation theory [15, 16].

The power transmission coefficient, T_p, which shows how much power is transmitted through an interface, is defined as:

$$T_p = 1 - \left(\frac{z_t/z_s - 1}{z_t/z_s + 1} \right)^2 \tag{6}$$

where z_t and z_s are mechanical impedances of the transmitter bar and specimen respectively. Mechanical impedance depends upon both the properties of the bar or specimen material and its physical dimensions:

$$z = A\rho c \tag{7}$$

A is the cross section area, ρ is material density and c the speed of sound in the material. The transmitter bar is made of a 16mm diameter titanium Ti-6Al-4V alloy (ρ=4506 kg/m^3, c=5030 m/s), thus (7) gives z_t=4557 kg/s.

The smallest cross section area in the specimen will determine the amount of power transmitted through. Hence we use the initial ligament for z_s calculations for all 4 specimens. This gives cross sections from 2 mm^2 to 8

mm^2. Using textbook values for steel - ρ=7850 kg/m^3, c=5172 m/s, 7 gives z_t from 81 to 325 kg/s. With that (6) gives T_p between 0.06 and 0.25. This means that in our experiments at best only a quarter of the pulse power reaches the strain gauge on the transmitted bar. In the worst case, for the specimen with 8 mm initial notch, only 6% of the pulse power reaches the strain gauge. Hence the signal/noise ratio on the transmitted strain gauge is poor.

Eqns. (6) and (7) clearly show how the stress signal/noise ratio, and hence the quality of the data collected in this work, can be improved. Either the specimen gauge section should be made thicker, or the incident and the transmitter bar should be made of smaller diameter and less dense material. However, care should be taken to insure the strains in both bars remain well below the elastic limit.

Shear damage initiation criterion [11] could be used in addition, or instead of, the ductile criterion adopted in this work. In shear damage initiation criterion the damage initiation strain is a function of strain rate and also of the shear stress ratio, $\theta_S = (q + k_s p)/\tau_{max}$, where τ_{max} is the maximum shear stress and k_s is a tunable material parameter. The shear criterion was not considered in this work because it's hard to achieve a variable shear stress ratio. This would require a dynamic specimen which can exhibit a wide range of maximum shear stresses. In addition the ductile criterion on its own is a better comparison with GTN, which does not take into account failure due to shear stresses. Nevertheless, measurement of shear stress ratio at high strain rates for consequent comparison with other damage models for axial crack propagation in pipes is an interesting future work.

It is unclear why G_F varies so much with strain rate. One direction for future work is to explore this further. To this end we would recommend keeping the notch length constant and vary the strain rate by varying only the gas pressure. In addition the shorter notches are probably preferable as they provide a longer crack propagation without the influence of necking effect.

8 Conclusions

A novel specimen geometry for the measurement of high strain rate flow and fracture properties of pipe materials has been proposed. With this specimen the flow and fracture properties of an X100 pipeline steel were measured with the split Hopkinson pressure bar at strain rates between 1207 s^{-1} and 2002 s^{-1}. The proposed specimen is well suited for the measurement of dynamic flow and fracture properties on X100 pipe material. The specimen is used on a conventional tensile split Hopkinson pressure bar machine. The specimen is easy to machine and can be cut straight from a pipe. One-dimensional theory can be used to approximate wave propagation in the specimen, even

though the stress distribution is non-uniform.

Video recording has proved very effective for the measurement of strain, however a rate of 400,000 frames per second is not high enough to observe the crack propagation.

Finite element modelling of the stress field in the specimen under the application of the boundary conditions at the specimen at fracture was used to calculate the fracture strain as a function of triaxiality.

Signal/noise ratio for the stress data is poor, due to a significant impedance mismatch between the transmitter bar and the specimen. Established techniques for minimising impedance mismatch, such as increasing the thickness of the specimen or using bars with lower density, should be tried in future work.

Significant variation of G_F with strain rate was observed. Not enough experimental data was collected to provide a convincing explanation of this effect, but it is believed that this effect has something to do with the notch length and the inconsistencies between the two-dimensional stress fields in the experiment and one-dimensional stress theory used to analyse the experimental results.

9 Acknowledgments

The authors would like to thank Prof J. R. Yates, at the time with the Mechanical Engineering Department, University of Sheffield, UK, for the provision of an X100 section used in our work. This work was supported by EPSRC through the Supergen 2 programme (GR/S86334/01 and EP/F029748/1).

References

[1] R. M. Andrews, N. Millwood, A. Batte, and B. Lowesmith. The fracture arrest behaviour of 914mm diameter X100 grade steel pipelines. In *ASME Proceedings of the 5th International Pipeline Conference*, pages 1693–1701, 2004.

[2] S. Igi, S. Kawaguchi, and N. Suzuki. Running ductile fracture analysis for JGA X80 burst test. In *Proceedings of 8th International Sympsium of the Japan Welding Society, 1*, pages 95–102, 2008.

[3] G. Mannucci and D. Harris. Fracture properties of API X100 gas pipeline steels. Technical Report EUR 20330 EN, European Commission, 2002.

[4] G. Demofonti, G. Mannucci, C. Spinelli, L. Barsanti, and H.-G. Hillenbrand. Large diameter X100 gas line pipes: fracture propagation

evaluated by full-scale burst test. Technical report, Europipe special reports, www.europipe.com, 2006.

[5] V. Tvergaard. Material failure by void growth to coalescence. *Advances in Applied Mechanics*, 27:83–151, 1990.

[6] A. Corigliano, G. Maier, and S. Mariani. Analysis of ductile fracture in damaged pipelines by a geometric parameter method. *Engineering Structures*, 21:924–936, 1999.

[7] F. Rivalin, J. Besson, A. Pineau, and M. Di Fant. Ductile tearing of pipeline-steel wide plates II. Modeling of in-plane crack propagation. *Engineering Fracture Mechanics*, 68(3):347–364, 2001.

[8] F. Dotta and C. Ruggieri. Structural integrity assessments of high pressure pipelines with axial flaws using a micromechanics model. *International Journal of Pressure Vessels and Piping*, 81(9):761–770, 2004.

[9] A. Hillerborg, M. Modéer, and P.-E. Petersson. Analysis of crack formation and crack growth in concrete by means of fracture mechanics and finite elements. *Cement and concrete research*, 6(6):773–781, 1976.

[10] H. Hooputra, H. Gese, H. Dell, and H. Werner. A comprehensive failure model for crashworthiness simulation of aluminium extrusions. *International Journal of Crashworthiness*, 9(5):449–463, 2004.

[11] Dassault Systèmes. Abaqus Analysis User's Manual, version 6.9, 2011.

[12] F. Oikonomidis. *Prediction of crack propagation in natural gas transmission pipelines by means of micromechanics and strain rate dependent models.* PhD thesis, Department of Mechanical Engineering, University of Bristol, 2010.

[13] Y. Bao and T. Wierzbicki. On fracture locus in the equivalent strain and stress triaxiality space. *International Journal of Mechanical Sciences*, 46:81–98, 2004.

[14] T. Wierzbicki, Y. B. Bao, Y. W. Lee, and Y. L. Bai. Calibration and evaluation of seven fracture models. *International Journal of Mechanical Sciences*, 47(4-5):719–743, 2005.

[15] W. Chen and Bo. Song. *Split Hopkinson (Kolsky) Bar.* Springer, 2011.

[16] B. A. Gama, Lopatnikov S. L., and J. W. Gillespie. Hopkinson bar experimental technique: a critical review. *Applied Mechanics Reviews*, 57(4):223–250, 2004.

[17] K. D. Potter and C. J. Setchell. Point-to-point non-contact video extensometry for composite materials and structures - a comparison with full-field methods. In *3rd International Conference on Composite Materials and Model Identification, Porto, Portugal*, 2006.

[18] S. H. Hashemi, I. C. Howard, J. R. Yates, R. M. Andrews, and A. M. Edwards. A single specimen CTOA test method for evaluating the crack tip opening angle in gas pipeline steels. In *ASME Proceedings of the 5th International Pipeline Conference*, pages 1703–1710, 2004.

[19] Y. Bai and T. Wierzbicki. Application of extended Mohr-Coulomb criterion to ductile fracture. *International Journal of Fracture*, 161:1–20, 2010.

[20] M. Dunand and D. Mohr. On the predictive capabilities of the shear modified Gurson and the modified Mohr-Coulomb fracture models over a wide range of stress triaxialities and Lode angles. *Journal of the Mechanics and Physics of Solids*, 59:1374–1394, 2011.

[21] M. Luo, M. Dunand, and D. Mohr. Experiments and modeling of anisotropic aluminum extrusions under multi-axial loading - Part II: Ductile fracture. *International Journal of Plasticity*, 32-33:36–58, 2012.